

MODELS OF JUPITER'S GROWTH INCORPORATING THERMAL AND HYDRODYNAMIC CONSTRAINTS[†]

JACK J. LISSAUER, OLENKA HUBICKYJ¹, GENNARO D'ANGELO²

NASA Ames Research Center, Space Science and Astrobiology Division, MS 245-3, Moffett Field, CA 94035, USA

AND

PETER BODENHEIMER

UCO/Lick Observatory, Department of Astronomy and Astrophysics, University of California, Santa Cruz, CA 95064, USA

October 23, 2018

ABSTRACT

We model the growth of Jupiter via core nucleated accretion, applying constraints from hydrodynamical processes that result from the disk–planet interaction. We compute the planet's internal structure using a well tested planetary formation code that is based upon a Henyey-type stellar evolution code. The planet's interactions with the protoplanetary disk are calculated using 3-D hydrodynamic simulations. Previous models of Jupiter's growth have taken the radius of the planet to be approximately one Hill sphere radius, R_H . However, 3-D hydrodynamic simulations show that only gas within $\sim 0.25 R_H$ remains bound to the planet, with the more distant gas eventually participating in the shear flow of the protoplanetary disk. Therefore in our new simulations, the planet's outer boundary is placed at the location where gas has the thermal energy to reach the portion of the flow not bound to the planet. We find that the smaller radius increases the time required for planetary growth by $\sim 5\%$. Thermal pressure limits the rate at which a planet less than a few dozen times as massive as Earth can accumulate gas from the protoplanetary disk, whereas hydrodynamics regulates the growth rate for more massive planets. Within a moderately viscous disk, the accretion rate peaks when the planet's mass is about equal to the mass of Saturn. In a less viscous disk hydrodynamical limits to accretion are smaller, and the accretion rate peaks at lower mass. Observations suggest that the typical lifetime of massive disks around young stellar objects is ~ 3 Myr. To account for the dissipation of such disks, we perform some of our simulations of Jupiter's growth within a disk whose surface gas density decreases on this timescale. In all of the cases that we simulate, the planet's effective radiating temperature rises to well above 1000 K soon after hydrodynamic limits begin to control the rate of gas accretion and the planet's distended envelope begins to contract. According to our simulations, proto-Jupiter's distended and thermally-supported envelope was too small to capture the planet's current retinue of irregular satellites as advocated by Pollack et al. [Pollack, J.B., Burns, J.A., Tauber, M.E., 1979. *Icarus* 37, 587–611].

Subject headings: Jovian planets; Jupiter, interior; Accretion; Planetary formation; Planet-disk interaction

1. INTRODUCTION

According to the core nucleated accretion model, giant planets begin their growth via the same process of agglomeration of solid bodies as do terrestrial planets; however, unlike terrestrials, the solid cores of giant planets reach masses large enough to capture substantial amounts of gas from their star's protoplanetary disk before said disk dissipates (Lissauer and Stevenson 2007). Previous models of this process have simulated either the thermal factors that limit the ability of a planet to retain gas (Bodenheimer and Pollack 1986, hereafter BP86; Pollack et al. 1996, hereafter PHBLPG96; Bodenheimer et al. 2000, hereafter BHL00; Ikoma et al. 2000; Hubickyj et al. 2005, hereafter HBL05; Alibert et al. 2005a,b; Marley et al. 2007) or the disk interaction physics that governs the flow of gas to a planet (Nelson et al. 2000;

D'Angelo et al. 2003, hereafter DKH03; Bate et al. 2003). Here we consider both thermal and gas flow limits to giant planet growth, and present the first models of the growth of Jupiter that are constrained by detailed simulations of both of these factors.

A planet of order one to several Earth masses (M_{\oplus}) at a distance of about 5 AU from the central star is able to capture an atmosphere from the protoplanetary disk because the escape speed from its surface is large compared to the thermal velocity of gas in the disk. However, such an atmosphere is very tenuous and distended, with thermal pressure pushing gas outwards and thereby limiting further accretion of gas. The key factor governing the ability of planet to accumulate additional gas when the mass of the atmosphere is less than the mass of the core is the planet's ability to radiate the energy that is provided to it by the accretion of planetesimals and gravitationally-induced compression of gas. The escape of this energy cools the gaseous envelope, allowing it to shrink and thereby enabling more gas to enter the planet's gravitational domain. Evolution occurs slowly, and hydrostatic structure is generally a very good approximation. Once a planet has enough mass for its self-gravity to compress the envelope substantially, its ability

Electronic address: Jack.Lissauer@nasa.gov
Electronic address: hubickyj@pollack.arc.nasa.gov
Electronic address: gennaro.dangelo@nasa.gov
Electronic address: peter@ucolick.org

¹ Also at UCO/Lick Observatory, University of California, Santa Cruz.

² NASA Postdoctoral Fellow.

[†] To appear in the journal ICARUS.

to accrete additional gas is limited only by the amount of gas available. Hydrodynamic limits allow quite rapid gas flow to a planet in an unperturbed disk. But a planet alters the disk by accreting material from it and by exerting gravitational torques upon it (Lin and Papaloizou 1979; Goldreich and Tremaine 1980). Both of these processes can lead to gap formation and isolation of the planet from the surrounding gas.

Our approach is to follow the physical structure and thermal evolution of the growing giant planet in the spherically symmetric (one-dimensional) quasi-hydrostatic approximation, and to incorporate the three-dimensional hydrodynamic interactions between the planet and the circumstellar disk via boundary conditions at the planet's outer 'surface'. Mass and energy transport within the planet are followed using the same planetary evolution code that we have employed in previous models of giant planet formation (BP86; PH-BLPG96; BHL00; HBL05; Marley et al. 2007).

Bodenheimer and Pollack (1986) prescribed the accretion rate of solids to be constant with time. Pollack et al. (1996) replaced this model by assuming that the planet was an isolated embryo that underwent runaway growth within a disk of dynamically cold, non-migrating, planetesimals. The accretion rate of solids depends upon the distribution of planetesimals as well as the planet's mass and its effective radius for accretion of planetesimals. The planet's capture cross-section was computed using the physical properties of the planet determined by the planetary structure calculation. The rate at which the planet accreted solids, \dot{M}_Z , for specified planet cross-section and disk surface density, eccentricities and inclinations of planetesimals within the planet's feeding zone, was determined using formulae that Greenzweig and Lissauer (1992) derived from 3-body numerical studies of planetesimal trajectories. This prescription has been used with slight modifications in most of our subsequent calculations, including all of those presented herein.

Our previous simulations have used simple *ad hoc* prescriptions for the interactions of the planet with the gaseous disk. We placed the outer boundary of the planet near its Hill sphere radius, R_H , during most of its growth. The radius of the planet's Hill sphere is given by:

$$R_H = r_p \left(\frac{M_p}{3 M_\star} \right)^{\frac{1}{3}}, \quad (1)$$

where M_p ($= M_{XY} + M_Z$) is the (gas + solids) mass of the planet, M_\star the mass of the star, and r_p is the orbital radius of the planet. More precisely, BHL00, HBL05, and Marley et al. (2007) took the planet's boundary to be the location where the thermal velocity of the H_2 gas molecules gave them sufficient energy to move upwards to $1 R_H$ from the planet's center. We limited the rate at which the planet could accrete gas from the disk to a maximum of $\sim 10^{-2} M_\oplus$ per year, which is approximately the Bondi rate. We extended many of our runs to a pre-determined mass limit of a Jupiter mass or more, and in a few cases we followed the ensuing phase of planetary contraction for 4.5 Gyr. But because of the approximate treatment of the later phases of gas accretion, we have always emphasized as our primary results the crossover time (when the planet's gas mass equals the mass of its condensables) and the corresponding crossover mass. The total formation time for the

planet is generally only slightly longer than the crossover time.

We present herein results of new simulations using our venerable 1-D planetary formation code to follow the evolution of the planet's structure, but now incorporating 3-D hydrodynamic calculations for prescriptions of the planet's size and maximum rates of gas accretion. In some of our calculations, we gradually reduce the density of gas within the surrounding disk to provide a more realistic simulation of the final phases of the planet's growth.

In the models presented herein, we neglect orbital migration. During the phase of runaway gas accretion, the amount of radial migration that is expected before the planet reaches one Jupiter-mass is on the order of 20% of its initial orbital radius (D'Angelo and Lubow 2008). Orbital decay due to resonant torques during the phase of slow gas accretion (Phase II) may be more substantial. However, a number of mechanisms may conspire to reduce those migration rates (see Papaloizou et al. 2007, for a review). There is presently a great deal of uncertainty surrounding these issues, so rather than rely on some poorly constrained and not yet well-understood migration mechanism, our simulations simply assume that the orbit of the planet remains fixed. The differing migration scenarios may affect giant planet growth in different ways, but our assumption of no migration is extreme in the sense that the isolation mass of a core within a planetesimal disk is larger for any non-zero migration of the planet, because the radial motion of the planet brings it into regions of the disk that are undepleted of planetesimals (Lissauer 1993; Alibert et al. 2005a). So migrating planets, or planetesimals migrating as a result of gas drag (Kary et al. 1993; Kary and Lissauer 1995), are likely capable of forming somewhat larger cores for a given location and disk surface mass density of solids than are the non-migrating planets that we simulate herein. Competing embryos in nearby accretion zones can act in the opposite sense from the above mentioned processes by removing solids from the planet's reach. But if the planet accretes an embryo, said embryo can bring with it solids from somewhat beyond the planet's nominal accretion zone.

Our 1-D accretion code is described in HBL05 and references therein. Details on the 3-D hydrodynamic numerical code can be found in DKH03 and references therein. We present our limits on the planet's physical extent and gas accretion rate, derived from 3-D hydrodynamic simulations, in Section 2. Section 3 discusses the physical parameters for our simulations. The results of our calculations are presented in Section 4. The scenario of capture of irregular satellites within proto-jupiter distended and thermally-supported envelope (Pollack et al. 1979) is discussed within the framework of our models for the growth of Jupiter in Section 5. We conclude in Section 6 with a discussion of our findings and their implications.

2. ENVELOPE SIZE AND MAXIMUM GAS ACCRETION RATES

Three-dimensional simulations of a disk with an embedded planet are used to estimate (i) the region of space within which gas is bound to a planetary core (Section 2.1) and (ii) the maximum accretion rate at which the disk can feed the inner parts of a growing planet's

Hill sphere (Section 2.2).

2.1. Outer Boundary of Planet’s Envelope

In order to evaluate the volume of gas that is gravitationally bound to a planet, we adopt disk models similar to those described in DKH03. The simulation region extends from 0 to 2π in azimuth and over a radial range from 2 to 13 AU, so that the disk boundaries are well separated from the planet’s orbit. The pressure scale height of the disk at the planet’s orbit, H_p , is taken to be 5% of the distance to the star; this corresponds to a temperature of $T = 115$ K for a gas of mean molecular weight 2.25 at a distance of 5.2 AU from a $1 M_\odot$ (solar mass) star. The dimensionless disk viscosity parameter is assumed to be $\alpha = 4 \times 10^{-3}$. We consider planet masses ranging from $10 M_\oplus$ to $50 M_\oplus$, because at smaller masses the planet’s envelope is very tenuous, and because at a mass exceeding $\sim 70 M_\oplus$ the planet self-compresses to a size much smaller than that of its Hill sphere. We use grid systems that resolve the mass density and the velocity field in the vicinity of the planet on length scales shorter than 4% of the Hill radius; thus the circumplanetary subdisk is also resolved. Simulations are started from an unperturbed Keplerian disk, whose rotation is corrected for effects of the gas pressure gradient. Models are evolved for about 250–300 orbital periods, at which time the flow has reached a quasi-stationary state. Tracer (massless) particles are deployed in the quasi-stationary flow, within a distance of approximately R_H from the core, and their trajectories are integrated for tens of orbital periods of the planet around the Sun. Several initial distributions of tracers are used, for purposes of a sensitivity study, containing from 500 to 6000 particles.

The tracers are advected by the flow field and a second-order Runge-Kutta algorithm is used to advance their position in time. Gas velocities are interpolated to the tracers’ positions via a monotonized harmonic mean (D’Angelo et al. 2002), which is second-order accurate and capable of dealing with large gradients and shock conditions. Therefore, the procedure is second-order accurate in both space and time.

We adopt a conservative approach to identify trajectories trapped inside the gravitational potential of the planet. Indicating with $s_i(t)$ the distance of the i -th particle from the center of the planet at time t , a tracer is marked as bound if $s_i(t)/s_i(0) < \zeta$ along its calculated trajectory, where $s_i(0) < R_H$. The number of bound tracers can grow as ζ increases because particles can temporarily move farther away from their deployment sites (i.e., $\zeta > 1$) before approaching the planet’s center and being finally accreted. However, the number of trapped trajectories is expected to eventually converge, upon increasing ζ , since particles that escape to librating or circulating orbits quickly move far away from the planet. Therefore, to select bound tracers, we increase the value of the parameter ζ until the number of selected trajectories does not change any longer, at which point we assume that the number of trapped particles has converged. Finally, we check that tracers discarded according to this procedure move out of the planet’s Hill sphere and thus return to the circumstellar disk. Note that the approach adopted here does not characterize as bound material gas that moves along trajectories originating outside of the Hill sphere and accreting onto the planet.

The initial distribution of bound particles is, in general, not spherically symmetric around the core, but it is roughly symmetric relative to the disk midplane, as displayed in Fig. 1. This figure shows positions (over about 3 orbital periods of the planet around the Sun) of tracers bound to a $10 M_\oplus$ (top) and a $30 M_\oplus$ (bottom) core and selected according to the procedure outlined above. The center of the planet is located at the origin of the axes and distances are normalized to R_H . Blue dots indicate positions with $s_i(t) < R_H/4$, whereas orange dots mark positions of particles trapped beyond $R_H/4$.

Given the necessity to describe the region containing bound particles with a single length for our 1-D planetary structure calculations, we estimate the radius of the largest sphere centered on the core and enclosed in the initial distribution of selected particles. This is done by considering the area obtained from the intersection of the volume occupied by selected particles with the disk midplane and evaluating the radius of the largest circle centered on the core and enclosed in this area. For the cases we investigate, we obtain a radius ranging from $\sim R_H/4$ to $\sim R_H/3$. An example is illustrated in Fig. 2. The left panel shows the initial positions of particles deployed close to the disk midplane and within $R_H/2$ of a $10 M_\oplus$ (top) and a $30 M_\oplus$ (bottom) core: blue circles represent bound tracers whereas orange circles represent particles that eventually escape from the core’s Hill sphere, as can be seen from their trajectories displayed in the right panel.

2.2. Gas Accretion Rates

We use the set of simulations in DKH03, together with analogous new simulations, to evaluate the maximum accretion rate at which a disk, perturbed by an embedded planet, can deliver gas to the planet’s vicinity. As before, we first consider disks with viscosity $\alpha = 4 \times 10^{-3}$ and local temperature $T = 115$ K. The numerical resolution is comparable to that of simulations discussed in the previous section. In these calculations, the accretion of gas proceeds almost uninhibited and is only limited by tidal effects (e.g., the formation of a density gap) or lack of supply from the disk. Therefore, accretion rates described in this section represent upper limits to the rate at which the disk can feed the inner parts of a planet’s Hill sphere.

We obtain gas accretion rates, \dot{M}_{XY} (M_{XY} denotes the mass of the H/He component of the planet), for planets ranging in mass from about $1 M_\oplus$ to $2 M_J$ (Jupiter masses). Data can be well fitted with a second-order polynomial written as

$$\log \left(\frac{\dot{M}_{XY}}{\Sigma_g r_p^2 / P} \right) \approx c_0 + c_1 \log \left(\frac{M_p}{M_\star} \right) + c_2 \log^2 \left(\frac{M_p}{M_\star} \right), \quad (2)$$

where Σ_g is the unperturbed surface density of gas at the orbital radius of the planet, r_p , and P is the planet’s orbital period. The coefficients are: $c_0 = -18.67$, $c_1 = -8.97$, and $c_2 = -1.23$. Gas accretion rates obtained from hydrodynamical models can be re-scaled by the initial mass density in the disk, at the planet’s orbital radius, because continuity and momentum equations that are solved in the calculations (see D’Angelo et al. 2005) can be normalized to an initial mass density

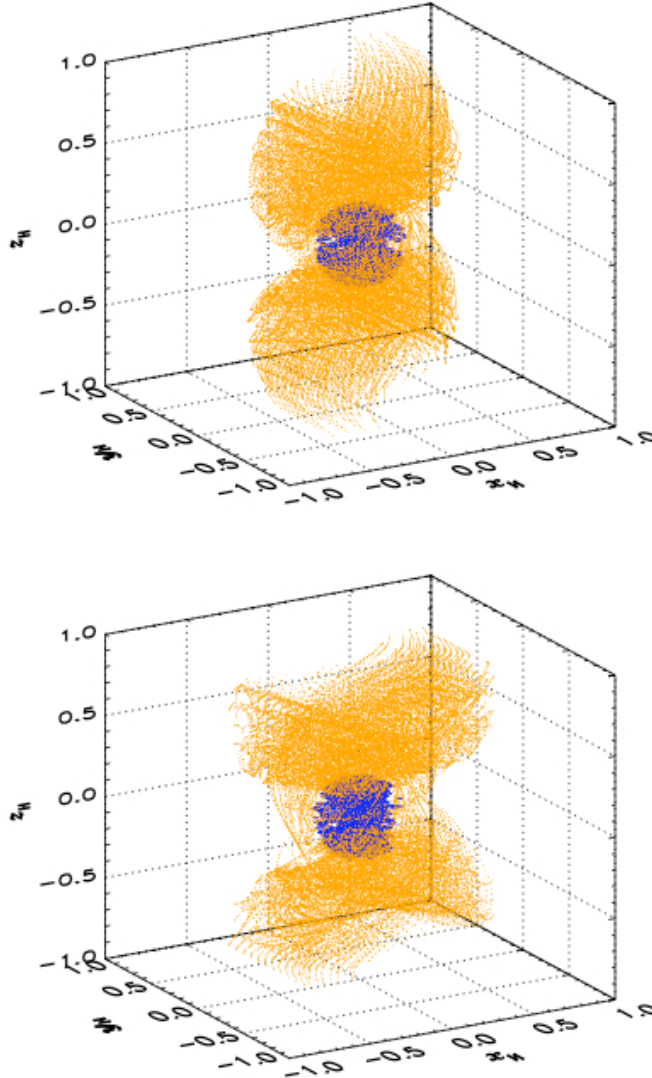


FIG. 1.— Trajectories in a frame rotating at the angular velocity of the planet (around the Sun) of ~ 2000 tracer particles that are bound to a $10 M_{\oplus}$ (top) and a $30 M_{\oplus}$ (bottom) point-mass planet, located at the origin. Bound particles were selected according to the procedure described in the text. Axes are in units of the Hill radius, R_H . Each dot marks the position occupied by a tracer at a given time. Positions within $R_H/4$ of the center of the planet are marked as blue dots, while positions beyond this distance are marked as orange dots.

(at r_p , for example) when pressure is directly proportional to mass density. Therefore, Eq. (2) can be used to derive a gas accretion rate as a function of the planet’s mass, its orbital radius, and the unperturbed surface density.

Although we were able to halt the accretion of the planet at Jupiter’s mass in a disk with $\alpha = 4 \times 10^{-3}$, this required either a very narrow gas feeding zone or a very special timing of disk dissipation (Section 4). Thus, in order to find a more plausible mechanism for forming Jupiter-mass planets, we modeled planetary growth within a lower viscosity protoplanetary disk. We performed simulations analogous to those described above for a planet within a disk of the same temperature but lower viscosity, $\alpha = 4 \times 10^{-4}$. The results for both viscosities are plotted in Fig. 3, together with the fit given by Eq. (2) for $\alpha = 4 \times 10^{-3}$ and a piecewise parabolic fit (not given here because it cannot be written in compact form) to accretion rates obtained from calculations

with $\alpha = 4 \times 10^{-4}$. In both cases, accretion rates account for surface density perturbations which depend on planet mass and disk viscosity. Note that planets in the lower viscosity disk cannot accrete gas as rapidly as planets of the same mass within a disk that is ten times as viscous. This is because density perturbations are stronger in the lower viscosity case, even at small planet masses. The difference in accretion rates is most profound for planets of Jupiter’s mass and larger. The shift of the peak accretion rates towards smaller planet masses as kinematic viscosity decreases is in qualitative agreement with the results of Tanigawa and Ikoma (2007).

So long as the gas density close to the planet’s orbit remains nearly undepleted, accretion rates in Fig. 3 can be understood in terms of gas accretion within the Bondi sphere, at a rate $\dot{M}_{XY} \propto M_p^3$ for $M_p/M_{\star} \lesssim (H_p/r_p)^3/\sqrt{3}$, and accretion within the Hill sphere at a rate $\dot{M}_{XY} \propto M_p$ for larger planet mass (see D’Angelo

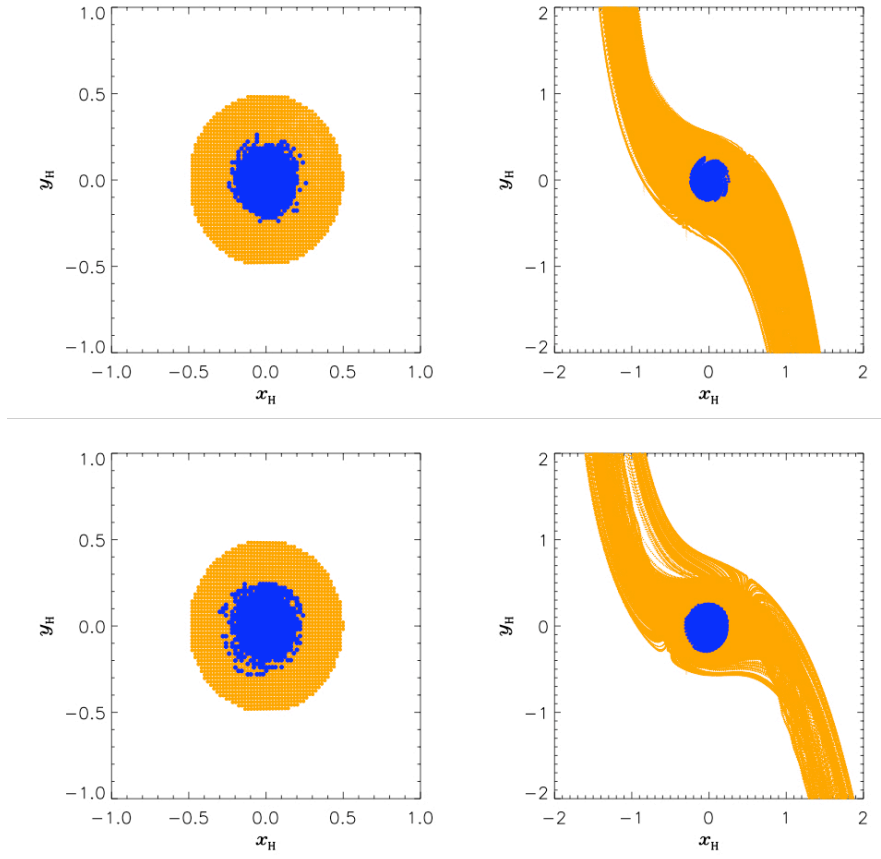


FIG. 2.— Initial positions (left) and trajectories (right), in a frame rotating at the angular velocity of the planet, of about 1000 tracer particles deployed close to the disk midplane and within $R_H/2$ of a $10 M_\oplus$ (top) and a $30 M_\oplus$ (bottom) point-mass planet located at the origin. Blue circles (left) and dots (right) indicate bound particles according to the procedure described in the text. Orange circles or dots represent particles that leave the planet’s Hill sphere and return to the circumstellar disk.

and Lubow 2008, for details). When density perturbations can no longer be neglected ($R_H \sim H_p$) and a gap starts to form, the accretion rate drops as the planet’s mass increases. The limiting gas accretion rates discussed here are not much affected by planet’s migration as long as the migration timescale is larger than the gap formation timescale.

2.3. Effects of Circumsolar Disk Hydrodynamics on Jupiter’s Accretion of Gas

We have modified our basic 1-D planet growth code to account for the limits of planet size and the supply of gas to the planet found with 3-D hydrodynamic calculations. As in BHL00 and HBL05, we define the accretion radius as

$$R_A = \frac{G M_p}{c_s^2/k_1 + G M_p/(k_2 R_H)}, \quad (3)$$

where c_s is the sound speed in the disk and k_1 and k_2 are constants. In the limit of large R_H , R_A reduces to k_1 times the Bondi accretion radius. In the limit of small R_H , R_A reduces to $k_2 R_H$. In previous studies, both k_1 and k_2 had been set to 1. In most of the simulations presented herein, we set $k_1 = 1$ and $k_2 = 1/4$, based on the calculations described in Section 2. When thermal factors limit the gas accretion rate, \dot{M}_{XY} is obtained through the requirement that the computed radius of the planet, R_p , actually matches R_A . When the hydrodynamics of the disk limits \dot{M}_{XY} , then the radius R_p

is determined by the procedure outlined in BHL00, and $R_p < R_A$.

In past work, the gas rate was arbitrarily capped at $1.053 \times 10^{-2} M_\oplus/\text{yr}$ to account for the Bondi accretion limit. In most of the present calculations, the hydrodynamic upper bound on the gas accretion rate is determined from the results shown in Fig. 3.

3. PARAMETERS OF OUR SIMULATIONS

In analogy with the principal simulation of HBL05, denoted 10L $^\infty$, all of our planetary evolution simulations are performed at 5.2 AU from a $1 M_\odot$ star within a disk that has an initial surface mass density of solids of 10 g cm^{-2} , which are in the form of 100 km radius planetesimals⁵, and of gas $\Sigma_g(t=0) = 700 \text{ g cm}^{-2}$. Also as in run 10L $^\infty$, we assume that the opacity due to grains

⁴ The run designator 10L $^\infty$ is used by HBL05 to denote that the surface density of solids is 10 g cm^{-2} , the dust opacity in the planet’s envelope is 2% that of the interstellar medium and there is no cutoff in accretion of planetesimals by the planet. As these three properties hold for all of the simulations presented herein, we use a new set of designators, discussed below, for all of our new runs.

⁵ As pointed out by Fortier et al. (2007), using a more physically sophisticated model to compute the eccentricities and inclinations of planetesimals (Kokubo and Ida 1998; Kokubo et al. 2000; Thommes et al. 2003) gives a lower value of \dot{M}_Z for a given planetesimal size. However, growth of the core is more rapid with smaller planetesimals (PHBLPG96; Fortier et al. 2007). Thus, our simulations probably correspond more closely to a disk of $\sim 1-$

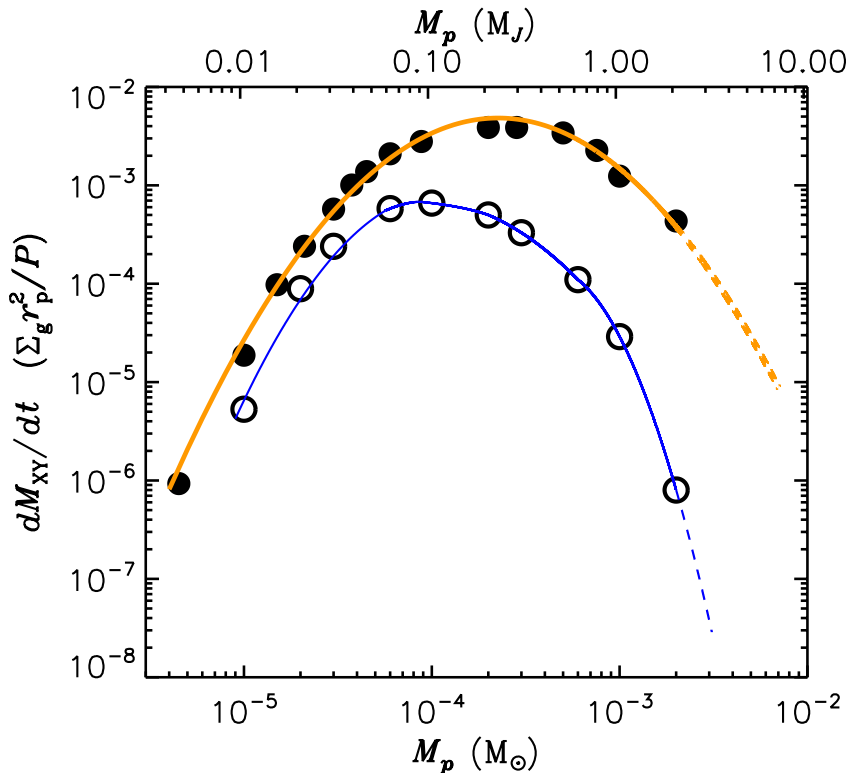


FIG. 3.— Limiting accretion rates as a function of the planet’s mass obtained from 3-D hydrodynamical calculations of a planet interacting with a circumstellar disk (see text for further details). Accretion rates are in units of the unperturbed surface density, Σ_g , at the planet’s orbital radius, r_p , and the planet’s orbital period, P . Filled circles correspond to results for a disk with a viscosity $\alpha = 4 \times 10^{-3}$ at the planet’s location. Empty circles are for a disk with $\alpha = 4 \times 10^{-4}$. The disk temperature at the orbital radius of the planet is $T \sim 100$ K. Masses on the lower axis are in units of the solar mass but they can be rescaled by the mass of the star, which is the unit of mass in the 3-D calculations. The thick orange curve represents a fit to the high viscosity data according to Eq. (2) and the appropriate coefficients. The thin blue curve is a piecewise parabolic fit to the low viscosity data.

within the growing planet’s envelope is 2% that of interstellar gas. In HBL05, we performed additional runs in order to examine the effects of differing values of the opacity of the planet’s atmosphere and the initial surface mass density of solids in the disk, and of terminating the accretion of solids prior to the termination of gas accretion. Herein, we study the orthogonal processes of (1) varying our prescription for the physical size of the planet’s envelope, (2) changing the formula for the maximum rate of gas accretion as a function of the planet’s mass, and (3) reducing the gas surface density of the protoplanetary disk as a function of time throughout the accretion epoch.

The sixteen new simulations (runs) that we report herein are divided into five groups. The input parameters for each of these runs are listed in Table 1.

In the three groups of runs whose labels begin with “1”, referred to collectively as “groups 1”, $T = 150$ K and the gas surface density remains constant throughout the computation, as in HBL05. The purpose of these simulations is to determine the effects of restricting gas flow onto the planet using the formula given by 3-D accretion simulations and/or reducing the radius of the outer

20 km radius planetesimals rather than the nominal size of 100 km. The sizes of the planetesimals in all of these models have been chosen in a largely *ad hoc* manner. A better estimate of \dot{M}_Z requires more sophisticated calculations in which planetesimal sizes and velocities are computed in a self-consistent manner rather than merely prescribed.

boundary of the planet’s envelope by up to a factor of four to account approximately for unbound protoplanetary disk gas flowing through the planet’s Hill sphere (Fig. 2). Specifically, Run 1G begins with the evolution found in 10L ∞ , but uses the gas flow limits from the 3-D calculations (Eq. 2) in place of the constant maximum gas accretion rate $\dot{M}_{XY} = 1.053 \times 10^{-2} M_{\oplus}$ per year that was inspired by a Bondi-type estimate and used in our previous studies. Run 1s uses the same formulation as 10L ∞ except that the planet’s accretion radius, R_A , (which prior to the onset of hydrodynamic limits to \dot{M}_{XY} lies at the outer boundary of the planet’s envelope) is placed at the radius where the gas has enough thermal energy to escape to $R_H/4$ rather than to R_H . Run 1sG has the same planet size as Run 1s and the same limits on gas flow as in simulation 1G. Run 1xsG provides a test of the sensitivity of moving the outer boundary of the envelope significantly inwards throughout the planet’s evolution. In Run 1xsG we (arbitrarily) set the outer boundary of the envelope to be 1/4 as far from the center of the planet as in 10L ∞ and use the same limits on the gas flow as in Runs 1G and 1sG (i.e., we set $k_1 = k_2 = 1/4$ in Eq. 3). In order to produce planets with mass equal to that of Jupiter, we taper off the accretion rate by multiplying the calculated maximum rate of gas accretion by a function which begins at unity when $M_p = 0.85 M_J$ and drops linearly with the planet’s mass so that it vanishes when $M_p = 1 M_J$; this is the same procedure as was used by HBL05.

TABLE 1
 INPUT PARAMETERS

Run	R_A	σ_{XY} (g/cm ²)	T_{neb} (K)	α	$\dot{M}_{XY,\text{limit}}$ (M _⊕ /yr)	limiting mass
10L [∞]	escape to R_H	700	150	—	1.053×10^{-2}	1 M _J
1G	escape to R_H	700	150	4×10^{-3}	Eq. (2)	1 M _J
1s	escape to $0.25 R_H$	700	150	—	1.053×10^{-2}	1 M _J
1sG	escape to $0.25 R_H$	700	150	4×10^{-3}	Eq. (2)	1 M _J
1xsG	$0.25 \times (\text{escape to } R_H)$	700	150	4×10^{-3}	Eq. (2)	1 M _J
2h	escape to $0.25 R_H$	700	115	4×10^{-3}	Eq. (2)	none
2hJ	escape to $0.25 R_H$	700	115	4×10^{-3}	Eq. (2)	1 M _J
2l	escape to $0.25 R_H$	700	115	4×10^{-4}	Fig. 3	none
2lJ	escape to $0.25 R_H$	700	115	4×10^{-4}	Fig. 3	1 M _J
3h	escape to $0.25 R_H$	Eq. (4)	115	4×10^{-3}	Eq. (2)	none
3hJ	escape to $0.25 R_H$	Eq. (4)	115	4×10^{-3}	Eq. (2)	1 M _J
3h4R _H	escape to $0.25 R_H$	Eq. (4) & $4R_H$	115	4×10^{-3}	Eq. (2)	none
3hR _H J	escape to $0.25 R_H$	Eq. (4) & $3.2R_H$	115	4×10^{-3}	Eq. (2)	1 M _J
3l	escape to $0.25 R_H$	Eq. (4)	115	4×10^{-4}	Fig. 3	none
3lJ	escape to $0.25 R_H$	Eq. (4)	115	4×10^{-4}	Fig. 3	1 M _J
3l4R _H	escape to $0.25 R_H$	Eq. (4) & $4R_H$	115	4×10^{-4}	Fig. 3	none
3lR _H J	escape to $0.25 R_H$	Eq. (4) & $11R_H$	115	4×10^{-4}	Fig. 3	1 M _J

All simulations in groups 2 and 3 assume the temperature of the disk (and thus at the upper boundary of the planet as long as the planet’s envelope remains in contact with the disk) is 115 K, the value used in the 3-D calculations for a gas of mean molecular weight 2.25. The planet radius prescription for all of these groups is the same as used for Runs 1s and 1sG.

In group 2, as in groups 1, the surface density of the gas remains constant at $\Sigma_g = 700 \text{ g cm}^{-2}$. In group 3, the surface density of gas within the disk drops linearly according to the formula:

$$\Sigma_g(t) = \begin{cases} 700 \text{ g cm}^{-2} \left(\frac{3 \text{ Myr} - t}{3 \text{ Myr}} \right) & \text{if } t \leq 3 \text{ Myr} \\ 0 & \text{if } t > 3 \text{ Myr} \end{cases} \quad (4)$$

The above equation accounts for disk dispersal in the planet formation region over timescales suggested by observations (Haisch et al. 2001) and recent theoretical models of disk photoevaporation due to combined action of FUV, EUV, and X-ray photons emitted by a solar-mass star (Gorti and Hollenbach 2008).

In the “h” runs within groups 2 and 3, the dimensionless disk viscosity is assumed to be $\alpha = 4 \times 10^{-3}$, and therefore the limiting gas accretion rate is taken from the 3-D calculations for disks with this viscosity (as in Runs 1G, 1sG and 1xsG), as given by Eq. (2). For the “l” runs within groups 2 and 3, the lower viscosity disk, $\alpha = 4 \times 10^{-4}$, is assumed, and the piecewise parabolic fits shown as a narrow blue curve in Fig. 3 are used for the upper bound of the planet’s gas accretion rate.

In Runs 3h and 3l, the planet continues to accrete for the entire 3 Myr that gas is assumed to be present. Analogously, the planet’s accretion is halted (in this case abruptly) after 3 Myr in Runs 2h and 2l. Accretion is terminated when the planet reaches 1 M_J in Runs 2hJ, 2lJ, 3hJ and 3lJ. For Runs 2hJ, 2lJ, and 3hJ, the same taper as used for groups 1 was applied, but using this prescription for Run 3lJ did not provide adequate mass to the planet, so we began the linear tapering when the planet mass was 0.975 M_J rather than 0.85 M_J.

We account for depletion of the gas in the disk via

accretion onto the planet as well as the linear decline from the overall dissipation of the protoplanetary disk in Runs 3h4R_H, 3hR_HJ, 3l4R_H and 3lR_HJ. However, gas pressure gradients can act to replace accreted gas, so rather than taking the gas loss rate within the planet’s gas feeding zone to be the sum of (i) the planet’s accretion of gas and (ii) the linear gas surface density drop-off rate assumed for the overall disk multiplied by the area of the planet’s gas feeding zone, we take the instantaneous gas loss rate to be the larger of these two quantities. We take the size of the planet’s gas feeding zone to be proportional to the size of its Hill sphere, so the gas feeding zone expands with the growth of the planet (Eq. 1) into regions not depleted by previous accretion by the planet. Note that these more distant regions are still affected by overall gas removal of the disk according to Eq. (4). We account for the expansion of the planet’s gas feeding zone similarly to our formula for computing the surface density of solids (Section 2.1 of PHBLPG96). In Runs 3h4R_H and 3l4R_H, the half-width of the planet’s gas accretion zone is taken to be $4 R_H$, the same as its solids accretion zone, and gas is allowed to accrete until there is no gas left. In Runs 3hR_HJ and 3lR_HJ, we choose (by an iterative procedure) the size of the gas accretion zone to be $3.2 R_H$ and $11 R_H$, respectively, so that the feeding zone runs out of gas when the planet’s mass is $\approx 1 M_J$.

4. RESULTS

In this section, we present the results of all of the simulations described in Section 3. Readers interested in a summary of these results may skip to Section 6, which includes a figure displaying the temporal evolution of the mass, radius and luminosity of the planet in what is probably our most physically realistic model of the growth of Jupiter, Run 3lR_HJ.

Within the five individual groups, all of the runs use the same computations for the initial phases of planet growth. Properties of the planet at milestone times during the early (thermally-regulated) phases of its growth

TABLE 2
RESULTS: PHASES I AND II

		10L [∞] /1G	1s/1sG	1xsG	2	3
FIRST LUMINOSITY PEAK	Time ^a	0.348	0.348	0.352	0.345	0.349
	M_Z ^b	7.98	8.04	8.15	8.06	8.35
	M_{XY} ^b	0.014	0.011	0.0093	0.013	0.014
	\dot{M}_Z	8.8×10^{-5}	8.8×10^{-5}	8.5×10^{-5}	8.8×10^{-5}	8.5×10^{-5}
	$\log L$ ^d	-5.05	-5.05	-5.06	-5.05	-5.05
	R_p ^e	41.53	25.56	10.51	29.08	29.62
END OF PHASE I	Time ^a	0.429	0.429	0.436	0.427	0.426
	M_Z ^b	11.49	11.47	11.47	11.49	11.48
	M_{XY} ^b	0.32	0.29	0.27	0.32	0.30
	\dot{M}_Z ^c	8.9×10^{-6}	8.7×10^{-6}	7.7×10^{-6}	8.5×10^{-6}	8.8×10^{-6}
	$\log L$ ^d	-5.90	-5.91	-5.95	-5.92	-5.90
	R_p ^e	56.78	31.34	14.23	34.90	36.24
MID PHASE II	Time ^a	1.59	1.69	1.86	1.61	1.63
	M_Z ^b	14.0	14.0	14.0	14.0	14.0
	M_{XY} ^b	7.0	7.0	7.0	7.0	7.0
	\dot{M}_Z	2.2×10^{-6}	2.0×10^{-6}	1.8×10^{-6}	2.2×10^{-6}	2.1×10^{-6}
	\dot{M}_{XY} ^c	7.8×10^{-6}	7.3×10^{-6}	6.5×10^{-6}	7.6×10^{-6}	7.4×10^{-6}
	$\log L$ ^d	-6.41	-6.45	-6.49	-6.44	-6.44
CROSSOVER POINT	Time ^a	2.28	2.38	2.59	2.30	2.32
	M_{cross} ^b	16.15	16.16	16.16	16.16	16.16
	\dot{M}_Z ^c	5.0×10^{-6}	5.4×10^{-6}	4.7×10^{-6}	5.4×10^{-6}	5.4×10^{-6}
	\dot{M}_{XY} ^c	2.7×10^{-5}	2.7×10^{-5}	2.3×10^{-5}	2.7×10^{-5}	2.7×10^{-5}
	$\log L$ ^d	-6.07	-6.08	-6.09	-6.07	-6.07
	R_p ^e	125.8	56.60	31.30	60.03	59.72
BIFURCATION	Time ^a	2.367	2.488	N/A	2.446	2.437

^a Time is in units of millions of years, Myr.

^b Mass is in units of Earth’s mass, M_{\oplus} .

^c The accretion rate is in units of Earth masses per year, M_{\oplus}/yr .

^d Luminosity is in units of solar luminosity, L_{\odot} .

^e Radius is in units of Jupiter’s present equatorial radius, R_J .

(denoted Phase I and Phase II) for all of the simulations are presented in Table 2. Note that for this epoch, only five simulations are required, and one of these is taken from the 10L[∞] run of HBL05. Table 2 also lists the “bifurcation” time, defined as the time at which the runs began to differ due to the differing assumptions regarding supply of gas to the planet. (The Run 1xsG has no bifurcation time because it was the only hypothesis considered within its group.) Analogous information for each of the runs at later times (at the onset of hydrodynamic limits to accretion, at maximum luminosity, and at the termination of accretion; Phase III) is displayed in Tables 3 and 4.

Let us first examine the values for the quantities that were key findings of previous simulations (PHBLPG96; BHL00; HBL05). These studies focused on the time required for the growth of the planet and the ultimate amount of condensable material in the planet. The crossover mass is almost identical in all of our present

runs (Table 2, Fig. 4), as expected since in our formulation the crossover mass depends almost entirely on the surface density of solids, the mass of the star and the distance of the planet from the star (see Eqs. 14 and 18 of PHBLPG96). The value that we find for M_Z at crossover, $16 M_{\oplus}$, is consistent with recent calculations of the mass of Jupiter’s core based upon Galileo data (Militzer et al. 2008); however other models yield smaller or no cores (Saumon and Guillot 2004). The time at which crossover is reached is about 10^5 years later in Run 1s/1sG than in 10L[∞]/1G as a result of the smaller planet size (and thus smaller radiating area, Table 2); note that the planet’s size is reduced by a larger factor late in the growth epoch. Crossover time is 3×10^5 years later in Run 1xsG than it is in 10L[∞]/1G, because the size of the planet is significantly smaller throughout accretion (Table 2). Thus, *reducing the planetary envelope’s outer radius by a factor of four has a nontrivial affect on the time that it takes for the planet to reach crossover, but*

TABLE 3
 RESULTS: PHASE III, GROUPS 1 & 2

		10L ∞	1G	1s	1sG	1xsG	2h	2hJ	2l	2lJ
ONSET OF LIMITED GAS ACCRETION	Time ^a	2.367	2.367	2.488	2.488	2.710	2.446		2.446	
	M_Z ^b	16.62	16.62	16.79	16.79	16.89	17.03		17.03	
	M_{XY} ^b	44.33	59.18	48.43	58.80	60.12	64.18		55.47	
	\dot{M}_{XY} ^c	0.0105	0.277	0.0105	0.277	0.277	0.275		0.0278	
	R_p ^e	182.7	163.2	76.0	52.3	34.3	68.0		72.8	
SECOND LUMINOSITY PEAK	Time ^a	2.368	2.368	2.507	2.488	2.710	2.447	2.447	2.451	
	M_{XY} ^b	254.3	215.2	254.2	144.8	180.0	290.7	252.2	123.9	
	$\log L$ ^d	-2.34	-1.47	-2.36	-1.53	-1.48	-1.43	-1.44	-2.78	
	R_p ^e	1.73	2.48	1.80	2.93	2.61	2.02	2.17	2.95	
ACCRETION STOPS	Time ^a	2.421	2.374	2.541	2.494	2.716	3.00	2.45	3.00	2.60
	M_Z ^b	16.89	16.65	17.10	16.83	16.93	20.36	17.07	20.36	17.96
	M_{XY} ^b	301.8	302.0	301.5	301.8	301.7	1810.0	301.6	525.0	300.0
	R_p ^e	1.63	1.76	1.68	1.74	1.68	1.34	1.74	1.57	1.78

^a Time is in units of millions of years, Myr.

^b Mass is in units of Earth's mass, M_\oplus .

^c The accretion rate is in units of Earth masses per year, M_\oplus/yr .

^d Luminosity is in units of solar luminosity, L_\odot .

^e Radius is in units of Jupiter's present equatorial radius, R_J .

 TABLE 4
 RESULTS: PHASE III, GROUPS 3

		3h	3hJ	3h4R _H	3hR _H J	3l	3lJ	3l4R _H	3lR _H J
ONSET OF LIMITED GAS ACCRETION	Time ^a	2.455	2.454	2.454	2.454	2.453	2.453	2.453	
	M_Z ^b	16.93	16.92	16.92	16.92	16.91	16.91	16.91	
	M_{XY} ^b	56.44	54.01	51.36	39.19	40.86	40.87		
	\dot{M}_{XY} ^c	0.0522	0.0471	0.0459	0.00596	0.00559	0.00582		
	R_p ^e	67.6	79.9	75.0	75.9	75.8	76.0		
SECOND LUMINOSITY PEAK	Time ^a	2.461	2.461	2.458	2.457	2.481	2.477	2.480	
	M_{XY} ^b	260.7	258.2	163.4	169.4	130.5	108.3	125.9	
	$\log L$ ^d	-2.07	-2.07	-2.41	-2.49	-3.48	-3.56	-3.51	
	R_p ^e	1.85	1.85	2.56	2.71	2.39	2.99	2.43	
ACCRETION STOPS	Time ^a	2.998	2.476	2.549	2.517	2.998	2.914	2.825	2.964
	M_Z ^b	20.12	17.05	17.49	17.30	20.18	19.68	19.15	19.98
	M_{XY} ^b	1072.0	301.6	385.6	301.0	309.1	297.8	244.1	297.6
	R_p ^e	1.39	1.67	1.66	1.72	1.62	1.64	1.80	1.64

^a Time is in units of millions of years, Myr.

^b Mass is in units of Earth's mass, M_\oplus .

^c The accretion rate is in units of Earth masses per year, M_\oplus/yr .

^d Luminosity is in units of solar luminosity, L_\odot .

^e Radius is in units of Jupiter's present equatorial radius, R_J .

accretion rates are not so sensitive to this parameter for our remaining uncertainty to be significant. Crossover occurs 8×10^4 years sooner in Runs 2 than in Runs 1s, implying that the lower disk temperature, which increases both the accretion radius, R_A , and the gas density at the planet's outer boundary, has a noticeable but not large effect on the growth rate. We found that this time was not very sensitive to gas density in BHL00 (compare Runs P1 and P2, wherein gas densities differ by three orders of magnitude), but the sensitivity of the formation

time to size of the planet's outer envelope boundary has not been previously studied.

Now let us turn to the growth of the planet at later times. These results are listed in Tables 3 and 4, and the masses and radii of the planet at late times are plotted in Fig. 6 and 7, respectively. In all cases, the planet's thermally regulated gas accretion becomes so rapid that flow from the disk limits the planet's growth rate $\sim 10^5$ years subsequent to crossover. The gas accretion rate of a planet with $M_p \gtrsim 50 M_\oplus$ that is well supplied by the

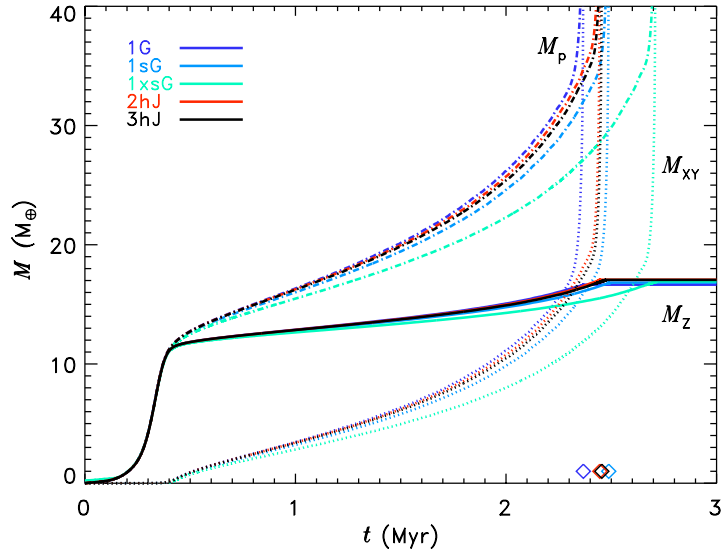


FIG. 4.— Mass of the giant planet as a function of time for the five runs listed in the color key, all of which use Eq. (2) to specify the hydrodynamic cap of gas accretion rates. Solid lines denote the mass of the condensible component of the planet, M_Z , dotted lines the H/He component, M_{XY} , and dot dashed lines the planet’s total mass, M_p . The ordinate is truncated at $40 M_\oplus$ in order to show details of the evolution prior to gas runaway. The bifurcation times for each of the four simulations with multiple endings are denoted by the diamonds situated just above the abscissa. Apart from small changes in the solid lines at later times and in the very last portions of some of the dotted lines, the results that are plotted here are applicable to all of the runs listed in Tables 3 and 4.

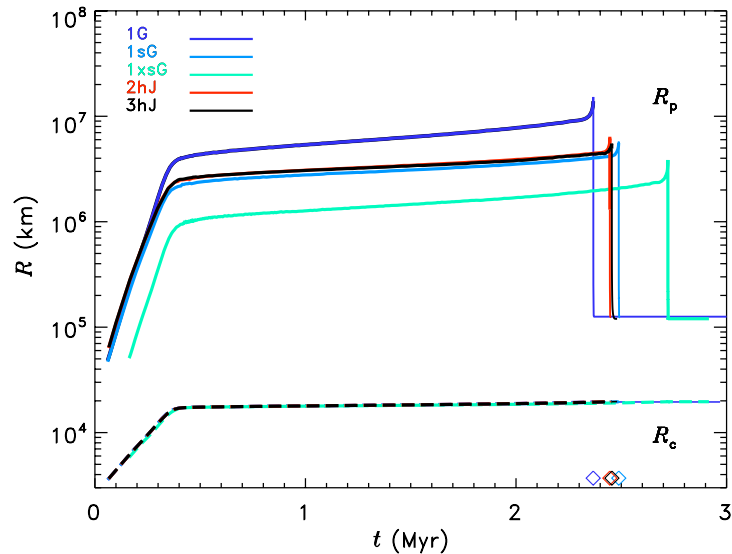


FIG. 5.— *Solid curves*: Outer radius of the planet as a function of time for the same five runs whose masses are shown in Fig. 4. The thicker portions of four curves correspond to times prior to the bifurcation of the runs. The primary differences between the planet’s radius from one run to another prior to the onset of limited gas accretion are direct consequences of the various prescriptions that were used for planetary radius (see Table 1). The slight differences in R_p among runs 1sG, 2hJ, and 3hJ result from differences in the growth rates of these planets (compare with Fig. 4). *Dashed curves*: The core radius, R_c , as a function of time for the same runs. As in Fig. 4, diamonds denote bifurcation times.

disk increases so rapidly that, within each of the four groups that bifurcated, the time at which disk-limited accretion set in varied by $\lesssim 2000$ years even though the

value of \dot{M}_{XY} at this milestone differed by more than an order of magnitude in some cases.

In our previous studies, the gas density in the disk

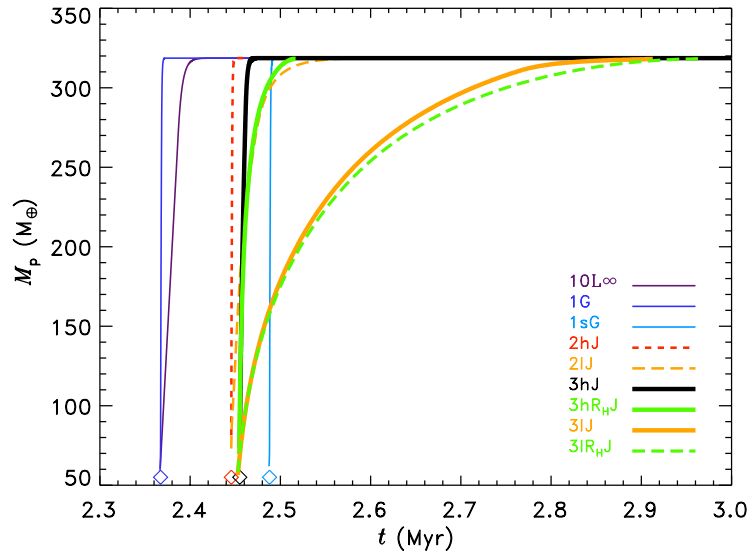


FIG. 6.— Total mass of the planet is shown at late times for the runs specified. Diamonds denote bifurcation times. Note that the lower value of the disk viscosity (Runs *2lJ*, *3lJ*, and *3lR_{HJ}*) produces more gradual (and we believe more realistic) termination of accretion for $1M_J$ planets.

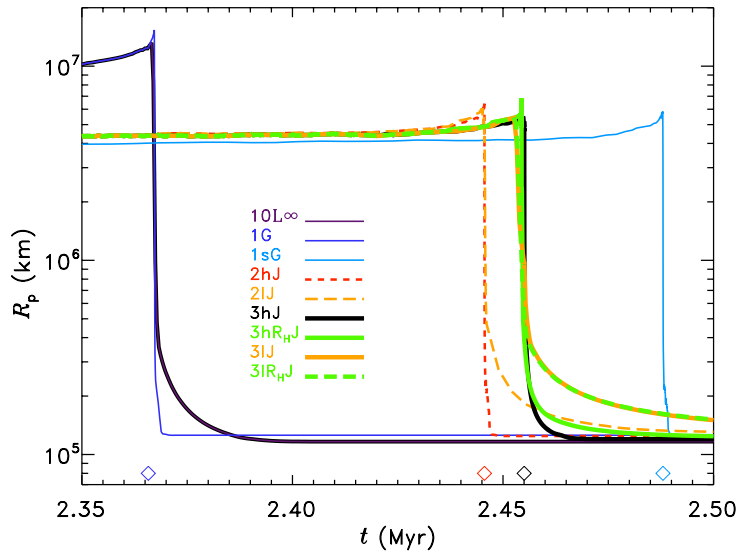


FIG. 7.— The outer radius of the planet as a function of time at late times, for the same runs whose late-time masses are displayed in Fig. 6. The radii of these planets change little during the interval $2.5 \text{ Myr} < t < 3 \text{ Myr}$ (not shown in the plot). Diamonds denote bifurcation times.

remained constant and the ability of a planet to accrete gas was a non-decreasing function of the planet's mass, so we needed to terminate accretion in a highly artificial manner. While accretion in many of the runs presented herein was terminated when the planet reached Jupiter's mass, in some runs we allowed the planet to accrete until the gas density in its vicinity dropped to zero after $\leq 3 \text{ Myr}$ had elapsed.

Runs *2h* and *2l* were stopped abruptly at 3 Myr, yielding planets of mass $1830 M_\oplus$ ($5.76 M_J$) and $525 M_\oplus$ ($1.65 M_J$), respectively. In Runs *3h* and *3l*, we assumed that removal of gas by the planet's accretion does not affect the gas surface density of the solar nebula in which the planet is embedded. As a result, planets of mass $1092 M_\oplus$ ($3.44 M_J$) and $324 M_\oplus$ ($1.02 M_J$) form by the time that the prescribed gas surface density of the neb-

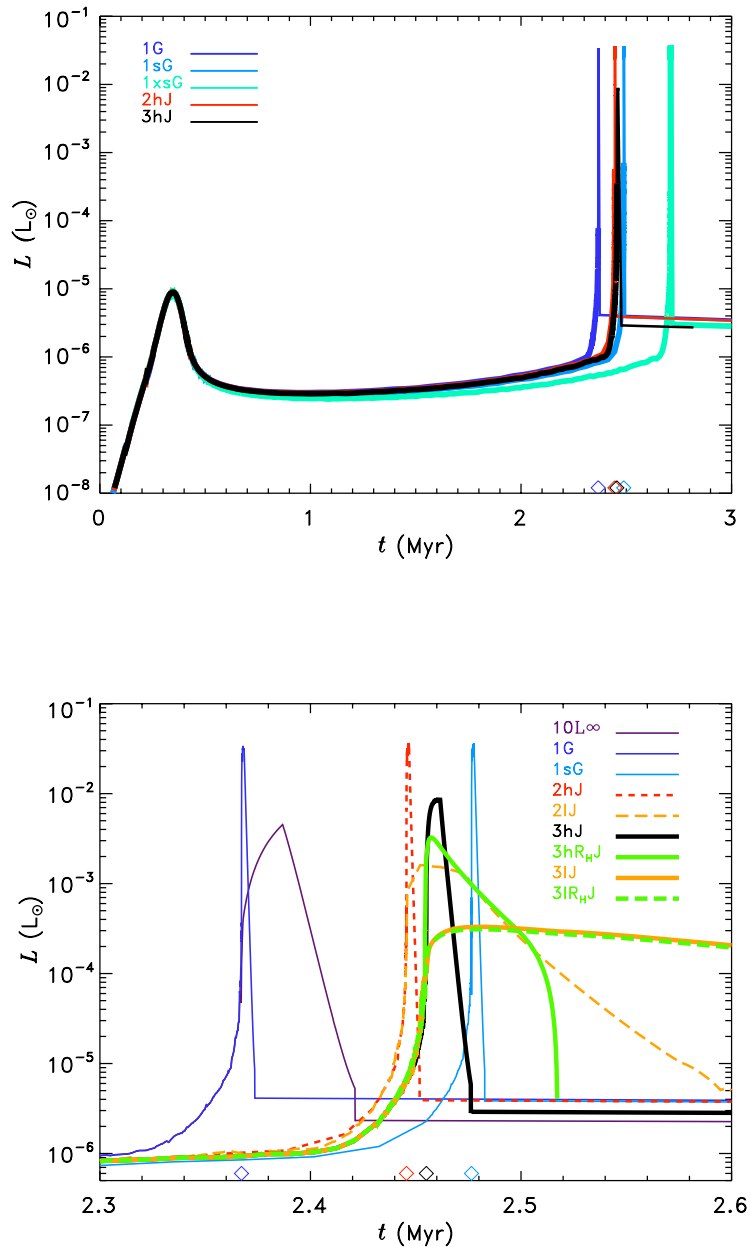


FIG. 8.— The planet’s luminosity as a function of time is shown for all of the runs which resulted in planets of mass equal to that of Jupiter. Diamonds denote bifurcation times. Top: The companion to Figs. 4 and 5, shows data from five pre-bifurcation runs as thick solid lines and post-bifurcation results from selected cases in high viscosity disks as narrow lines. Bottom: The companion to Figs. 6 and 7, shows the post-bifurcation luminosity of nine runs that produce planets of mass $1 M_J$. Note in all cases the step increase in luminosity as the rate of gas accretion accelerates after crossover; this is a real physical consequence of the core nucleated accretion model of giant planet formation. The value at which luminosity peaks depends upon the planetary mass at which disk hydrodynamics begins to limit the rate of mass accretion, and thus on the viscosity and surface density of the disk in the vicinity of the planet. Those simulations in which accretion of gas is tapered off exhibit a corresponding taper in luminosity; the curve for run $3lR_{HJ}$ is probably most realistic, as this run has the most plausible treatment of the tail off in gas accretion.

ula dropped to zero at 3 Myr.

In half of the runs in group 3 (those whose designation includes “ R_H ”), the surface density of gas in the planet’s accretion zone drops as gas is accreted by the planet. During most of the formation epoch, the planet’s accretion rate of gas is smaller than the removal of gas from its feeding zone by the overall depletion of our pro-

toplanetary disk. Thus, planetary removal of gas in Runs $3h4R_H$ and $3hR_{HJ}$ does not affect the planet’s growth in our algorithm during this interval. Indeed, for the first 2.437 Myr, one numerical calculation suffices to follow all eight runs in group 3. However, when the planet begins to rapidly accrete gas, the surface density of gas within the planet’s feeding zone drops rapidly, de-

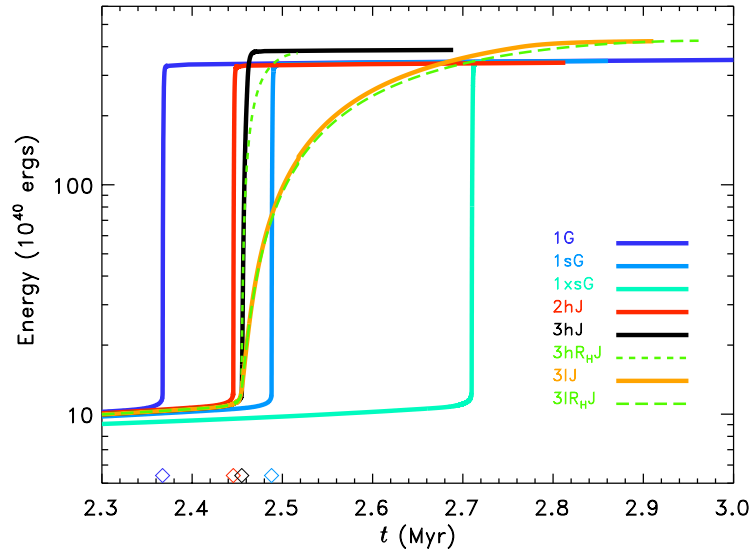


FIG. 9.— Integrated luminosity (i.e., total energy radiated) of the planet from the start of the simulation is shown as a function of time for the runs which produced Jupiter mass planets. Most of the energy is emitted during the epoch when the planet accretes the bulk of its gas. This epoch is very similar (albeit displaced somewhat in time) for runs 1G, 1sG, 1xsG and 2hJ, so the total energy radiated in these runs is almost the same. Accretion of gas near the luminosity peak is slower in the group 3 runs because the surface density is lower (and, in some cases, the viscosity is also lower); this allows the planet to radiate more energy. Diamonds denote bifurcation times.

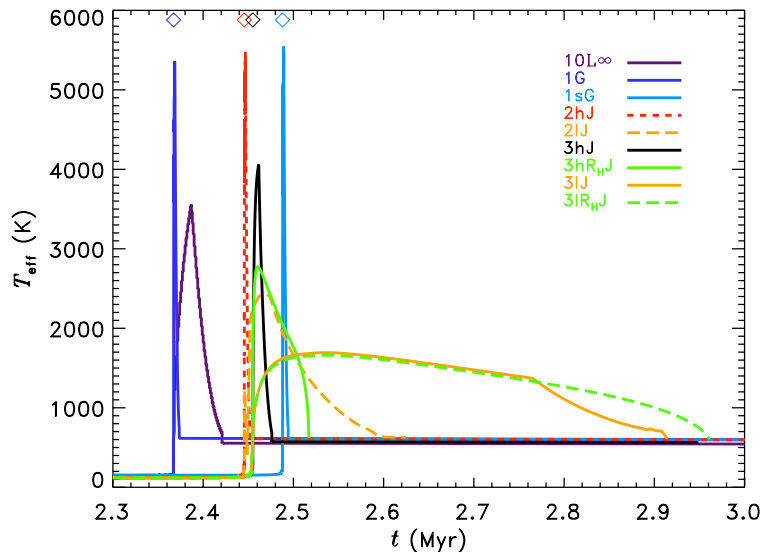


FIG. 10.— The effective temperature of the planet during and subsequent to the late phases of accretion for the runs indicated. Note that in the most realistic runs, for which accretion tapers off gradually, the planet has a lower peak temperature, but it remains quite warm for longer periods of time. The diamonds near the top left denote the bifurcation times.

spite the addition of gas via the expansion of the feeding zone. This leads to a decline in \dot{M}_{XY} . Eventually, the accretion of gas by the planet becomes so small that the rate of decrease in gas surface density in the planet's accretion zone is less than the prescribed overall linear decline rate. At this point, we switch back to the linear

drop-off (i.e., \dot{M}_{XY} within the feeding zone being given by the derivative of Eq. (4) multiplied by the area of the feeding zone, plus a small addition of gas as a result of feeding zone expansion into regions of the disk that have not been depleted of gas via the planet's accretion). The run ends when the gas density in the feeding zone drops

to zero. In Run $3h4R_H$, the planet grows to $403 M_\oplus$ ($1.27 M_J$) in 2.549 Myr and in Run $3l4R_H$ the planet reaches $263 M_\oplus$ ($0.83 M_J$) in 2.825 Myr. In Run $3hR_HJ$, we reduce the size of the gas accretion zone to $3.2 R_H$ so that the planet runs out of gas when its mass is $\sim 1 M_J$. Likewise, in Run $3lR_HJ$ we increase the size of the zone to $11 R_H$ to give the same final mass.

The planet radiates away much of the gravitational energy released by accretion and contraction, and therefore it is quite luminous during most of the accretionary epoch. The planet's luminosity throughout its growth is shown in Fig. 8 (top) for five cases which use the high viscosity disk formula to specify the hydrodynamic limit to gas accretion and which end with a Jupiter-mass planet. Peak luminosity values (see also Tables 3 and 4) are very similar for all of these runs apart from $3hJ$, which has a smaller peak because the surface density of gas of the disk is much lower during the late stages of planetary accretion. Figure 8 (bottom) displays the planet's luminosity after bifurcation for selected runs that ended with a $1 M_J$ planet. The luminosity peak in run 1G is higher but narrower than in $10L^\infty$ because the specified hydrodynamic limit to accretion is larger. Likewise, the luminosity peaks for the $3h$ runs are higher and narrower than those of the $3l$ runs because of more rapid gas accretion. Slower accretion is also responsible for the slightly lower luminosity peaks for the ' R_H ' runs compared to the runs with the same viscosity that do not account for disk depletion resulting from planetary accretion.

Note that the peak luminosity can be very high, up to $10^{-1.5} L_\odot$ in Run 1G, but the width of the peak is very short in runs where the peak is high. During the planet's high luminosity phase, it heats the gas in its neighborhood of the circumstellar disk. However, as hydrodynamic factors (rather than thermal ones) limit the planet's accretion at this epoch, \dot{M}_{XY} should not be significantly reduced. The total energy liberated during the rapid gas accretion phase is about the same in all cases (Fig. 9), so in Run $3lR_HJ$, for example, the peak luminosity is $10^{-3.5} L_\odot$, but the phase lasts for almost 4×10^5 years.

The integrated luminosity of the planet up to the time of crossover in every case is $\sim 10^{41}$ ergs. The integrated luminosity for the entire accretionary epoch for all cases that produce a $1 M_J$ planet is $3 - 4 \times 10^{42}$ ergs, with most of this being radiated during the (in some cases very) brief accretionary spike. The final gravitational potential energy of each of these $1 M_J$ planets is close to -1.5×10^{43} ergs. The integrated luminosity is significantly less than half the absolute value of the gravitational potential energy because dissociation of hydrogen absorbs a substantial amount of energy; the virial theorem for self-gravitating bodies is not violated.

The effective temperature of a forming Jupiter-like planet is of interest to observers searching from thermal radiation of such objects. We show $T_{\text{eff}} \equiv [L/(4\pi R_p^2 \sigma_{\text{rad}})]^{1/4}$ for several cases in Figure 10.

5. IMPLICATIONS FOR CAPTURE OF IRREGULAR SATELLITES

The irregular satellites of the giant planets are clearly captured objects (e.g., Peale 2007). The semimajor axes of the orbits of all but 2 of the 54 known jovian irreg-

ular satellites are between 150 and $350 R_J$; the orbital periods of these objects range from 8 months to a little over 2 years. An object approaching from heliocentric orbit has positive energy with respect to Jupiter (i.e., the magnitude of their kinetic energy exceeds that of their gravitational binding energy to Jupiter). Three-body effects caused by the combined perturbations of the Sun and Jupiter near the boundary of Jupiter's Hill sphere can reverse this balance, leading to temporary capture into jovacentric orbit (e.g., Kary and Dones 1996). Permanent capture requires that a non-conservative process acts while the body is in the vicinity of Jupiter.

Addition of mass to Jupiter increases the depth of the planet's gravitational potential well. Jupiter's Hill sphere expands (see Eq. 1), and orbiting objects conserve angular momentum as the planet accretes additional material. Assuming that the orbital period of a moon is short compared to the timescale of the increase of the planet's mass, eccentricity is conserved and the semimajor axis of the orbit goes as M_p^{-1} . Objects captured when Jupiter was significantly less massive than it is today thus would orbit well within the current planet's Hill sphere, because their immediate post-capture orbits would have been within the smaller Hill sphere of the growing planet and the orbits would have shrunk during Jupiter's later accretion of matter. (Exceptions would be objects captured into distant quasi-satellite orbits which fortuitously crossed the narrow bridge in phase space connecting them with retrograde orbits as the planet grew and those whose orbits were altered by collisions, etc.)

No proposed mechanism for capture of small satellites by giant planets is fully satisfactory (Jewitt and Haghighipour 2007). The viability of two of the leading theories for the capture of irregular satellites (apart from Neptune's anomalous large irregular moon, Triton) can be assessed within the framework of our model of giant planet growth. These capture theories involve: (i) reduction of kinetic energy via gas drag within primordial circumplanetary envelopes shortly before these envelopes collapsed (Pollack et al. 1979); and (ii) increase in the magnitude of the gravitational potential energy via rapid mass accretion by Jupiter (Heppenheimer and Porco 1977).

Pollack et al. (1979) used Bodenheimer's (1977) model of the evolution of giant planet envelopes. According to Bodenheimer's model, Jupiter collapsed hydrodynamically from a size of $\sim 225 R_J$ to $\sim 30 R_J$ on a timescale of $\sim 1-2$ years, and this process occurred after the planet had reached its present mass, $1 M_J$. Planetesimals entering the envelope shortly before this collapse could have lost enough kinetic energy via gas drag to be captured, but not so much as to spiral too deeply into the planet's gravitational potential well. Our present model of giant planet formation differs substantially from that prevailing three decades ago, and we show below that capture of the observed irregular satellites by gas drag in the extended envelope of proto-Jupiter is not consistent with the planet growth simulations presented in Section 4.

The giant planet formation models presented herein have three major differences from those of Bodenheimer (1977) that make irregular satellite capture in the extended and thermally-supported envelope phase difficult. Firstly, the envelope collapses gradually, over a timescale

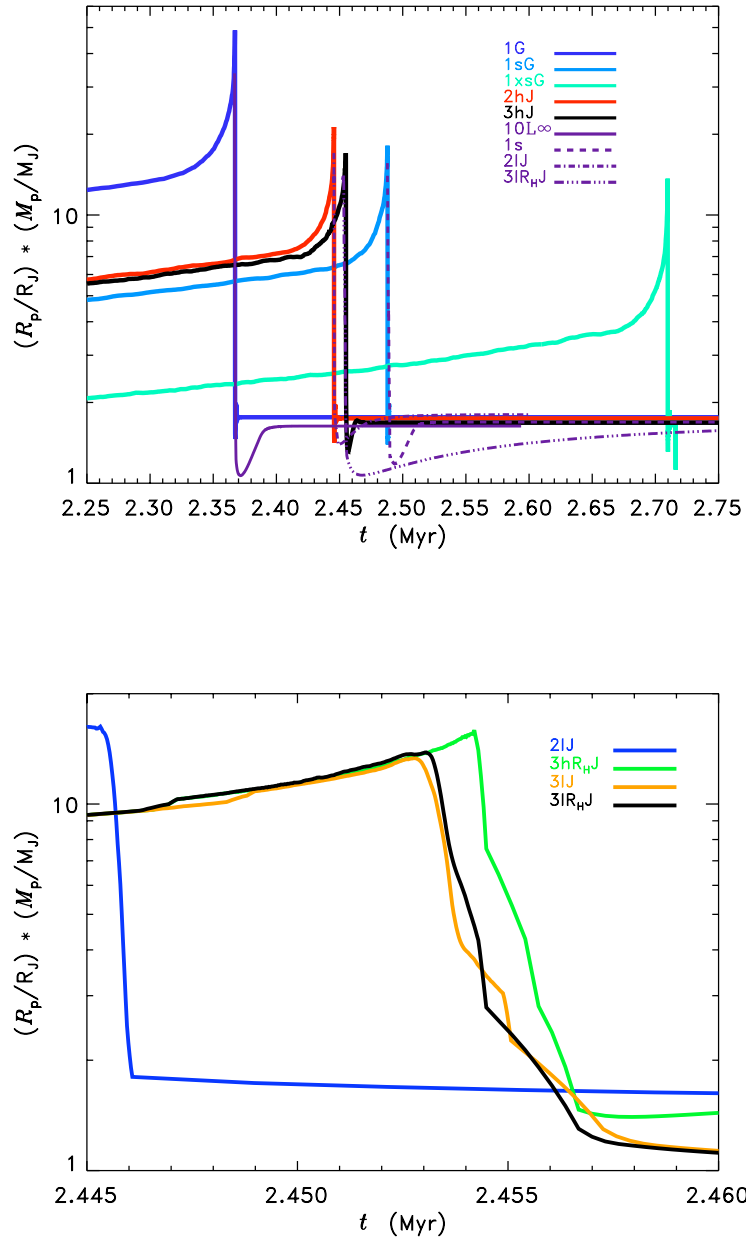


FIG. 11.— The final orbital distance that a test particle orbiting at the outer boundary of the planet at the time specified would have at the end of the accretion epoch if the only orbit-altering effect was shrinkage to conserve orbital angular momentum as the planet grew to a mass of $1 M_J$. Top: Late Phase II and Phase III for each of the five groups, with two variants shown for three of the four groups that bifurcated. Apart from Runs 10L $_{\infty}$ and 1G, which we view to be among the least realistic runs of this paper (because of the large assumed size of the planet and high disk viscosity), the peak value is $\lesssim 20 R_J$. Note that all of the curves end at values of $\sim 1.7 R_J$, because in our model $1 M_J$ planets are about this radius at the termination of accretion (Tables 3 and 4). Bottom: Close-up values near the peak for the four most physically realistic runs presented in this paper. The characteristic shrinking times range from a few hundred to a few thousand years.

of a few centuries to a few millennia for cases (Fig. 11, bottom) in which the most realistic assumptions of the rate that the disk supplies gas to the planet are made (and over decades in some of the less physically plausible runs) rather than hydrodynamically; this makes survival of captured satellites against spiraling into the planet questionable. Secondly, the planet’s envelope collapses when the planet’s mass is only about $0.25 M_J$ (Tables 3

and 4); so orbits of bound bodies would shrink substantially due to the continued accretion of mass by the planet. Thirdly the size of the planet’s envelope prior to collapse is only $\lesssim 80 R_J$ for all runs that use the prescription for planet radius given by the hydrodynamic simulations presented in Section 2.

The latter two differences imply that satellites captured during Jupiter’s extended and thermally-supported

envelope phase would orbit far closer to the planets than do the observed irregulars. The maximum size of the envelope (which is the size prior to collapse) is smaller than calculated by Bodenheimer (1977) both because the envelope collapses at smaller planetary mass and because in our new models the envelope is restricted by gas flow in the protoplanetary disk to a region only $\sim 1/4$ th as large as that of their Hill radius (Fig. 1 and 2). We plot in Fig. 11 the temporal evolution of a ‘scaled radius’, $\mathcal{R}_p \equiv R_p M_p/M_J$, which is the post-accretion perijove distance of a body on an orbit just tangent to the outer radius of the protoplanet at the time in question⁶. The value of \mathcal{R}_p peaks below $50 R_J$ in all of our runs and below $20 R_J$ in the most realistic runs (Fig. 11, bottom).

The simulations of the growth of Jupiter presented herein are thus inconsistent with the model of capture of Jupiter’s irregular satellites within proto-Jupiter’s distended and thermally-supported envelope. Our calculations do not address (and therefore do not exclude) the possibility that the irregular satellites were captured as a result of gas drag within a circumjovian disk. Additionally, the accretion timescale during the epoch when the planet accumulates the bulk of its mass is short compared to the planet’s overall growth time, yet too long compared to trapping times for temporary capture of particles by Jupiter for the Heppenheimer and Porco (1977) model to be viable.

6. SUMMARY AND CONCLUSIONS

We have modeled the growth of Jupiter incorporating both thermal and hydrodynamic constraints on its accretion of gas from the circumsolar disk. Our study included simulations of planets growing in disks of high and low viscosity; the surface mass density of gas within the disk remained constant in some cases and decreased gradually in others (see Table 1 for details). The most physically plausible model of the formation of Jupiter included herein is Run 3/R_HJ, in which the dimensionless disk viscosity is $\alpha = 4 \times 10^{-4}$ and the surface density of the gas within the disk decreases with time, thereby allowing a gradual tapering off of gas accretion as the planet approaches its ultimate mass. Results of this simulation are presented in Figure 12.

The principal results of our investigation are: (1) Three dimensional hydrodynamic calculations show that the flow of gas in the circumsolar disk limits the region occupied by the planet’s tenuous gaseous envelope to within $\sim 0.25 R_H$ (Hill sphere radii) of the planet’s center, which is much smaller than the value of $\sim 1 R_H$ that was assumed in previous studies. (2) This smaller size of the planet’s envelope increases the planet’s accretion time, but only by ~ 5 –10%. In general, in agreement with previous results (HBL05), Jupiter formation times are in the range 2.5–3 Myr, assuming a protoplanetary disk with solid surface density of 10 g cm^{-2} and dust opacity in the protoplanet’s envelope equal to 2% that of interstellar material. (3) In a protoplanetary disk whose dimension-

⁶ This assumes that the accreting gas does not collide with the satellites, leading to gas drag and further shrinking satellite orbits, and that accretion is slow compared to the orbital period of the satellites. The most rapid rate of increase in Jupiter’s mass depends upon the viscosity in the surrounding protoplanetary disk (Fig. 3 and Table 3). For the more viscous case that we studied, the planet’s mass increases at up to $\sim 0.3\%$ per year.

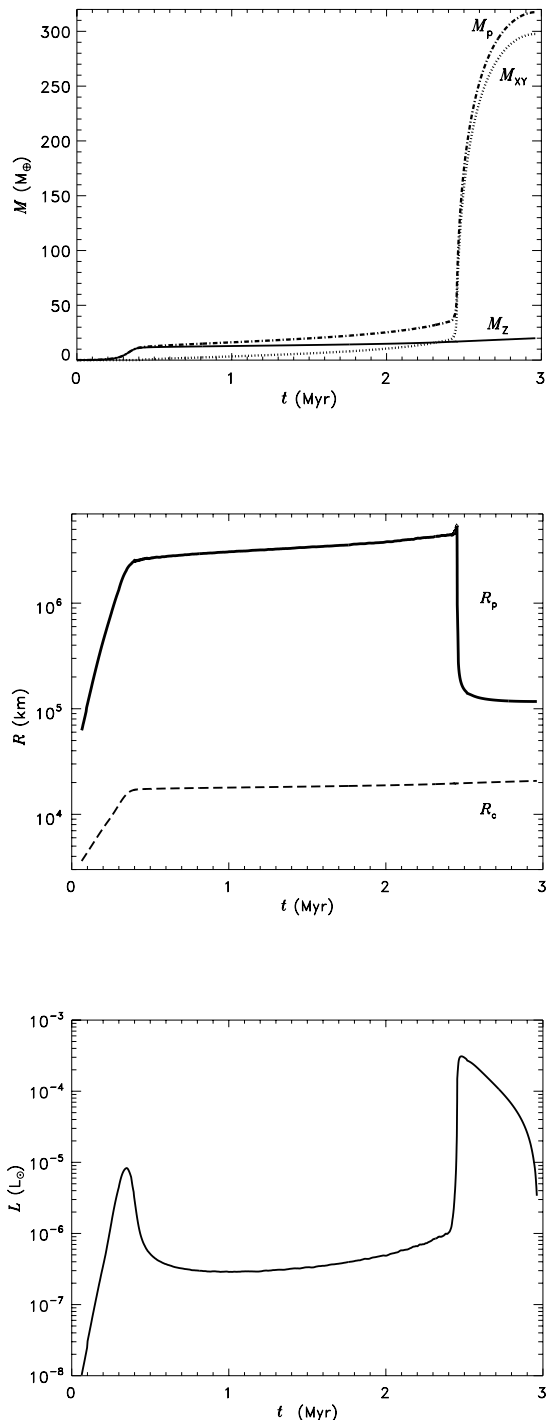


FIG. 12.— The temporal evolution of the planet according to our most physically realistic case, Run 3/R_HJ (see Tables 1, 2, and 4 for details). Top: The mass of solids in the planet (solid line), gas in the planet (dotted line) and the total mass of the planet (dot-dashed line) are shown as functions of time. Note the slow, gradually increasing, buildup of gas, leading to a rapid growth spurt, followed by a slow tail off in accretion. Middle: The radius of the planet (solid line) and that of the planet’s heavy element core (dashed line) are shown as functions of time. Note the logarithmic scale used for radius. Bottom: The planet’s luminosity is shown as a function of time. The rapid contraction of the planet just before $t = 2.5$ Myr coincides with its highest luminosity and the epoch of most rapid gas accretion.

less viscosity parameter $\alpha \sim 4 \times 10^{-3}$, giant planets grow to several times the mass of Jupiter unless the disk has a small local surface density when the planet begins to accrete gas hydrodynamically, or the disk is dispersed very soon thereafter. The large number of planets known with masses near Jupiter compared with the smaller number of substantially more massive planets (Udry and Santos 2007) is more naturally explained by planetary growth within circumstellar disks whose dimensionless viscosity parameter is $\alpha \sim 4 \times 10^{-4}$. (4) Capture of Jupiter's irregular satellites within the planet's diffuse and distended thermally-supported envelope is not consistent with the Jupiter formation models presented herein.

We thank Jeff Cuzzi and two anonymous referees for providing valuable comments. Primary support for this study was provided by NASA's Outer Planets Research Program grant 344-30-99-02; additional support came from NASA Origins of Solar Systems grant NNX08AH82G. GD is supported through the NASA Postdoctoral Program. Computational resources for the 3-D hydrodynamic calculations were provided by the NASA High-End Computing Program systems under grants SMD-06-0181 and SMD-07-0372.

REFERENCES

Alibert, Y., Mordasini, C., Benz, W., Winisdoerffer, C., 2005a. Models of giant planet formation with migration and disc evolution. *Astron. Astrophys.* 434, 343–353. 1, 2

Alibert, Y., Mousis, O., Mordasini, C., Benz, W., 2005b. New Jupiter and Saturn formation models meet observations. *Astrophys. J.* 626, L57–L60. 1

Bate, M. R., Lubow, S. H., Ogilvie, G. I., Miller, K. A., 2003. Three-dimensional calculations of high- and low-mass planets embedded in protoplanetary discs. *Mon. Not. R. Astron. Soc.* 341, 213–229. 1

Bodenheimer, P., 1977. Calculations of the effects of angular momentum on the early evolution of Jupiter. *Icarus* 31, 356–368. 14, 16

Bodenheimer, P., Hubickyj, O., Lissauer, J. J., 2000. Models of the in situ formation of detected extrasolar giant planets. *Icarus* 143, 2–14. (BHL00) 1, 2, 5, 8, 9

Bodenheimer, P., Pollack, J. B., 1986. Calculations of the accretion and evolution of giant planets: the effects of solid cores. *Icarus* 67, 391–408. (BP86) 1, 2

D'Angelo, G., Bate, M. R., Lubow, S. H., 2005. The dependence of protoplanet migration rates on co-orbital torques. *Mon. Not. R. Astron. Soc.* 358, 316–332. 3

D'Angelo, G., Henning, T., Kley, W., 2002. Nested-grid calculations of disk-planet interaction. *Astron. Astrophys.* 385, 647–670. 3

D'Angelo, G., Kley, W., Henning, T., 2003. Orbital migration and mass accretion of protoplanets in three-dimensional global computations with nested grids. *Astrophys. J.* 586, 540–561. (DKH03) 1, 2, 3

D'Angelo, G., Lubow, S. H., 2008. Evolution of migrating planets undergoing gas accretion. *Astrophys. J.* 685, 560–583. 2, 4

Fortier, A., Benvenuto, O. G., Brunini, A., 2007. Oligarchic planetesimal accretion and giant planet formation. *Astron. Astrophys.* 473, 311–322. 5

Goldreich, P., Tremaine, S., 1980. Disk-satellite interactions. *Astrophys. J.* 241, 425–441. 2

Gorti, U., Hollenbach, D., 2008. Photoevaporation of circumstellar disks by FUV, EUV and X-ray radiation from the central star. *Astrophys. J.* in press. 7

Greenzweig, Y., Lissauer, J. J., 1992. Accretion rates of protoplanets. II - Gaussian distributions of planetesimal velocities. *Icarus* 100, 440–463. 2

Haisch, K. E., Lada, E. A., Lada, C. J., 2001. Disk frequencies and lifetimes in young clusters. *Astrophys. J.* 553, L153–L156. 7

Heppenheimer, T. A., Porco, C., 1977. New contributions to the problem of capture. *Icarus* 30, 385–401. 14, 16

Hubickyj, O., Bodenheimer, P., Lissauer, J. J., 2005. Accretion of the gaseous envelope of Jupiter around a 5–10 Earth-mass core. *Icarus* 179, 415–431. (HBL05) 1, 2, 5, 6, 8, 16

Ikoma, M., Nakazawa, K., Emori, H., 2000. Formation of giant planets: dependences on core accretion rate and grain opacity. *Astrophys. J.* 537, 1013–1025. 1

Jewitt, D., Haghighipour, N., 2007. Irregular satellites of the planets: products of capture in the early solar system. *Annu. Rev. Astron. Astrophys.* 45, 261–295. 14

Kary, D. M., Dones, L., 1996. Capture statistics of short-period comets: implications for Comet D/Shoemaker-Levy 9. *Icarus* 121, 207–224. 14

Kary, D. M., Lissauer, J. J., 1995. Nebular gas drag and planetary accretion. II. Planet on an eccentric orbit. *Icarus* 117, 1–24. 2

Kary, D. M., Lissauer, J. J., Greenzweig, Y., 1993. Nebular gas drag and planetary accretion. *Icarus* 106, 288–307. 2

Kokubo, E., Ida, S., 1998. Oligarchic growth of protoplanets. *Icarus* 131, 171–178. 5

Kokubo, E., Ida, S., Makino, J., 2000. Evolution of a circumterrestrial disk and formation of a single moon. *Icarus* 148, 419–436. 5

Lin, D. N. C., Papaloizou, J., 1979. Tidal torques on accretion discs in binary systems with extreme mass ratios. *Mon. Not. R. Astron. Soc.* 186, 799–812. 2

Lissauer, J. J., 1993. Planet formation. *Annu. Rev. Astron. Astrophys.* 31, 129–174. 2

Lissauer, J. J., Stevenson, D. J., 2007. Formation of giant planets. In: Reipurth, B., Jewitt, D., Keil, K. (Eds.), *Protostars and Planets V*. pp. 591–606. 1

Marley, M. S., Fortney, J. J., Hubickyj, O., Bodenheimer, P., Lissauer, J. J., 2007. On the luminosity of young jupiters. *Astrophys. J.* 655, 541–549. 1, 2

Militzer, B., Hubbard, W. B., Vorberger, J., Tamblin, I., Bonev, S. A., 2008. A massive core in Jupiter predicted from first-principles simulations. *ArXiv e-prints* 807. 8

Nelson, R. P., Papaloizou, J. C. B., Masset, F., Kley, W., 2000. The migration and growth of protoplanets in protostellar discs. *Mon. Not. R. Astron. Soc.* 318, 18–36. 1

Papaloizou, J. C. B., Nelson, R. P., Kley, W., Masset, F. S., Artymowicz, P., 2007. Disk-planet interactions during planet formation. In: Reipurth, B., Jewitt, D., Keil, K. (Eds.), *Protostars and Planets V*. pp. 655–668. 2

Peale, S. J., 2007. The origin of the natural satellites. In: Spohn, T. (Ed.), *Treatise on Geophysics*. Vol. 10. Elsevier, Amsterdam, pp. 465–508. 14

Pollack, J. B., Burns, J. A., Tauber, M. E., 1979. Gas drag in primordial circumplanetary envelopes - A mechanism for satellite capture. *Icarus* 37, 587–611. 2, 14

Pollack, J. B., Hubickyj, O., Bodenheimer, P., Lissauer, J. J., Podolak, M., Greenzweig, Y., 1996. Formation of the giant planets by concurrent accretion of solids and gas. *Icarus* 124, 62–85. (PHBLPG96) 1, 2, 5, 7, 8

Saumon, D., Guillot, T., 2004. Shock compression of deuterium and the interiors of Jupiter and Saturn. *Astrophys. J.* 609, 1170–1180. 8

Tanigawa, T., Ikoma, M., 2007. A systematic study of the final masses of gas giant planets. *Astrophys. J.* 667, 557–570. 4

Thommes, E. W., Duncan, M. J., Levison, H. F., 2003. Oligarchic growth of giant planets. *Icarus* 161, 431–455. 5

Udry, S., Santos, N. C., 2007. Statistical properties of exoplanets. *Annu. Rev. Astron. Astrophys.* 45, 397–439. 17